Composite Structures 201 (2018) 121–130

Contents lists available at ScienceDirect

Composite Structures

journal homepage: www.elsevier.com/locate/compstruct

# A novel composite multi-layer piezoelectric energy harvester

Qingqing Lu[a,c], Liwu Liu[b], Fabrizio Scarpa[c,d,*], Jinsong Leng[a], Yanju Liu[b,*]

[a] Centre for Composite Materials, Science Park of Harbin Institute of Technology (HIT), P.O. Box 3011, No. 2 YiKuang Street, Harbin 150080, People's Republic of China
[b] Department of Astronautical Science and Mechanics, Harbin Institute of Technology (HIT), P.O. Box 301, No. 92 West Dazhi Street, Harbin 150001, People's Republic of China
[c] Bristol Composites Institute (ACCIS), University of Bristol, Bristol BS8 1TR, UK
[d] Dynamics and Control Research Group (DCRG), CAME, University of Bristol, BS8 1TR, UK

ARTICLE INFO

*Keywords:*
Piezoelectric energy harvesting
Composites beam
Vibration energy harvester

ABSTRACT

A typical linear piezoelectric energy harvester (PEH) is represented by a unimorph or bimorph cantilever beam. To improve the efficiency of linear PEHs, classical strategies involve the increase of the beam length, tapering or adding additional cantilever beams to the free end. In this work we discuss the design of novel type of composite linear multi-layer piezoelectric energy harvester (MPEH). MPEHs here consist of carbon fibre laminates used as conducting layers, and glass fibre laminas as insulating components. We develop first a electromechanical model of the MPEH with parallel connection of PZT layers based on Euler-Bernoulli beam theory. The voltage and beam motion equations are obtained for harmonic excitations at arbitrary frequencies, and the coupling effect can be obtained from the response of the system. A direct comparison between MPEH and PEH configurations is performed both from the simulation (analytical and numerical) and experimental point of views. The experiments agree well with the model developed, and show that a MPEH configuration with the same flexural stiffness of a PEH can generate up to 1.98–2.5 times higher voltage output than a typical piezoelectric energy harvester with the same load resistance.

## 1. Introduction

The development of wireless sensor networks and the reduction of their power requirements has significantly driven research activities related to vibration piezoelectric energy harvesting technologies, which possess high energy conversion efficiencies from mechanical vibrations to electrical power, all within the use of simple designs [1]. In 1996, Williams and Yates first introduced the concept of vibration energy harvesting [2]. Wang et al. (1999) then presented the constitutive equations of symmetrical triple layer piezoelectric benders, and introduced different types of piezoelectric benders, like unimorphs and bimorphs with series or parallel connection [3]. Erturk and Inman have established the fundamental electromechanical model of a piezoelectric cantilever beam, with their 2008 papers related to a single-degree-of-freedom (SDOF) harvester beam with one PZT layer [4,5]. The same Authors then investigated the analytical model of bimorph cantilever configurations with series and parallel connections of PZT layers [6]. Micro-fibre composites (MFC) can also be used in vibration energy harvesters. Song et al. developed the theoretical model for energy harvesting devices with two types of MFC materials, and the influence of the beam thickness, natural frequency and electrical resistance were also experimental investigated [7]. Nonlinear PEHs have been additionally designed and developed in recent years to expand the operational frequency bandwidth. Erturk et al. [8,9] have presented a nonlinear broadband piezoelectric power generator with two magnets near the free end of the cantilever beam and with two piezoelectric layers on the surface. The piezo-magnetoelastic configuration proposed could generate a power one order of magnitude larger than the one provided by a linear PEH at several frequencies. The performance of a nonlinear magnetopiezoelastic energy harvester driven by random excitations was described by Litak et al. [10] and Ali et al. [11]. Their work shows that it is possible to optimally design the system by using analytical techniques, such that the mean harvested power is maximized for a given strength of the input broadband random ambient excitation. Ferrari et al. utilized two layers of PZT films to fabricate a piezoelectric bimorph, and the resulting nonlinear converter proposed implements nonlinearity and bistability by using a single external magnet [12]. Friswell et al. have also designed a new type of highly nonlinear piezoelectric cantilever beam, exhibiting two potential wells with large tip masses, when the beam is buckled [13]. Other nonlinear PEHs with magnets can be found in Refs. [14–16], and in the review article [17]. Betts et al. presents an arrangement of bistable composite

* Corresponding authors at: Bristol Composites Institute (ACCIS), University of Bristol, Bristol BS8 1TR, UK (F. Scarpa).
*E-mail addresses:* f.scarpa@bristol.ac.uk (F. Scarpa), yj_liu@hit.edu.cn (Y. Liu).

https://doi.org/10.1016/j.compstruct.2018.06.024
Received 2 March 2018; Accepted 6 June 2018

plates with bonded piezoelectric patches to perform broadband vibration-based energy harvesting from ambient mechanical vibrations [18]. Arrieta et al. have designed a cantilevered piezoelectric bi-stable composite concept for broadband energy harvesting with two piezoelectric layers attached on the surface of bistable composites [19]. Pan et al. used bistable hybrid symmetric laminates to make a broadband piezoelectric energy harvester, and have discussed the influence of the lay-up design on the performance of the bistable PEH [20,21]. Qi et al. have designed a multi-resonant beam with piezoelectric fibre composites (PFC) to produce a broadband PEH [22]. A double cantilever energy harvester was evaluated via a distributed parameter modelling and experimental tests by Rafique et al. [23]. Adhikari et al. have used a stack configuration piezoelectric energy harvester, and generated power from broadband vibration [24]. Paknejad et al. have presented a distributed parameter electroelastic model for various multilayer composite beams and discussed the influence of the composites layups [25]. Akbar et al. have studied the dynamic response of piezoelectric energy harvesters embedded in a wingbox structure [26]. Some new piezoelectric energy harvester configurations have also been presented to improve the efficiency during vibration, such as the L-shape [27], the V-shape [28] and the compressive-mode energy PEHs [29].

From the above literature review it is possible to observe that both linear and nonlinear PEHs are in general designed using a symmetrical triple layer structure (i.e., one mid-structure with two piezo-layers on the surfaces). This baseline configuration has been modified by using different beam/plate lengths or shapes (tapering), however the fundamental layout remains the same. In this study we propose a PEH structure with a more complex through-the-thickness topology. The electromechanical model of the composite multi-layer piezoelectric energy harvester (MPEH) is here established based on the use of the Euler-Bernoulli beam theory. The fundamental natural frequency and the power output of the MPEH beam are then extracted, and the performance of the MPEH is discussed based on simulations and experimental data. A parametric analysis of the voltage density and resonant frequencies is also performed versus different stacking sequences of the MPEHs and PEHs leading to different specific flexural stiffness (i.e., normalized by the mass of the beams). From the simulations, experimental data and the parametric analysis we will demonstrate that the MPEHs can generate significantly more power than the PEHs configurations, in particular for small specific flexural stiffness configurations. The variations of the natural frequencies in MPEHs and PEHs with similar specific flexural stiffness are less pronounced, with the PEHs having larger fundamental natural frequencies compared to the MPEHs cases.

## 2. Analytical electro-mechanical model

Fig. 1 presents the design of the MPEH, which consists of multiple PZT layers and composites laminates. The MPEH is a cantilever beam with carbon fibres, glass fibres laminates and PZT layers. The length of cantilever beam is L, and b is the width. Fig. 1(b) and (c) represent the cross section of the MPEH, $h_{ci}$, $h_{cj}$ are the thickness of the carbon fibre laminates, $h_{gi}$ is the thickness of the glass fibre laminate. The thickness of the PZT layer is $h_p$, and $h_s$ is the total thickness of the beam except for the external layers PZT. In the design, the polarization direction for all the PZT layers is the same, which means that each pair of PZT layers are connected in parallel. The carbon fibre laminates are here used as conducting layers, and the glass fibre laminates constitute the insulating layers.

### 2.1. Basic equations and fundamental natural frequency

The thickness is relatively small than the length of the composite beam, so the general governing equation of motion of an Euler-Bernoulli beam with embedded piezoelectric layers can be written as [6],

$$\frac{\partial^2 M(x,t)}{\partial x^2} + c_s I\frac{\partial^5 w(x,t)}{\partial x^4 \partial t} + c_a\frac{\partial w(x,t)}{\partial t} + m\frac{\partial^2 w(x,t)}{\partial t^2} = -(m + M_t)\frac{\partial^2 w_b(x,t)}{\partial t^2} \tag{1}$$

In Eq. (1), $M(x,t)$ is the bending moment of the beam; $w(x,t)$ is the beam transverse deflection relative to its base, and $w_b(x,t)$ is the base excitation motion on the beam along the z-direction. The tip mass at $x = L$ is $M_t$. The bending moment can be related to the internal stresses of the layers in the following manner:

$$\begin{aligned} M(x,t) &= -b\int_{t_c}\sigma_c z dz - b\int_{t_g}\sigma_g z dz - b\int_{t_p}\sigma_p z dz \\ &= -b\sum_{k=1}^{N_c}\int_{t_{ck}}\sigma_c z dz - b\sum_{k=1}^{N_g}\int_{t_{gk}}\sigma_g z dz - b\sum_{k=1}^{N_p}\int_{t_{pk}}\sigma_p z dz \end{aligned} \tag{2}$$

In Eq. (2), $\sigma_c$, $\sigma_g$, $\sigma_p$ correspond to the normal stress of carbon and glass fibre laminates, and of the piezoelectric layers along the x-axis, respectively. For the $k$th layer of the elastic composite laminate, the bending stress is defined:

$$(\sigma_c, \sigma_g)_k = -z(\overline{Q}_{11})_k\frac{\partial^2 w}{\partial x^2} \tag{3}$$

The $k$th layer stiffness $\overline{Q}_{11}$ can be defined by using the traditional classical laminate theory [30]:

$$\begin{aligned} \overline{Q}_{11} &= Q_{11}\cos^4\theta + 2(Q_{12} + 2Q_{66})\sin^2\theta\cos^2\theta + Q_{22}\sin^4\theta \\ Q_{11} &= \frac{E_1}{1-\nu_{12}\nu_{21}} \\ Q_{12} &= \frac{\nu_{12}E_2}{1-\nu_{12}\nu_{21}} \\ Q_{22} &= \frac{E_2}{1-\nu_{12}\nu_{21}} \\ Q_{66} &= G_{12} \end{aligned} \tag{4}$$

where $E_1$ is the Young's modulus along the fibre direction, $E_2$ is the Young's modulus along the transverse direction, and $G_{12}$ is the shear modulus. The Poisson's ratios are $\nu_{12}$ and $\nu_{21}$, and $\theta$ is the fibre orientation.

The stress in the PZT layer can be expressed by the constitutive equations for a piezoelectric slab:

$$\sigma_p = E_p\varepsilon_1^p(x,t) - \bar{e}_{31}E_3(t) \tag{5}$$

In Eq. (5) $E_p$ is the elastic modulus of piezoelectric layer, $\varepsilon_1^p$ is the axial strain components, $\bar{e}_{31}$ is the piezoelectric constant and $E_3$ is the electric field across the thickness of the beam.

From the Euler-Bernoulli beam theory, the internal bending moment can be obtained by substituting Eqs. (3), (5) into Eq. (2):

$$M(x,t) = -YI\frac{\partial^2 w(x,t)}{\partial x^2} + \vartheta_p[H(x) - H(x-L)] \tag{6}$$

where $YI$ is the flexural rigidity of the piezoelectric elastic composites. The Heaviside function $H(x)$ limits the location of the piezoelectric layer along the x-direction on the host structure. The flexural rigidity can be described by:

$$\begin{aligned} YI = b\sum_{k=1}^{N_c}(\overline{Q}_{11})_k^c\int_{z_{k-1}}^{z_k} z^2 dz + b\sum_{k=1}^{N_g}(\overline{Q}_{11})_k^g\int_{z_{k-1}}^{z_k} z^2 dz \\ + E_p b\sum_{i=1}^{N_p}\int_{z_{k-1}}^{z_k} z^2 dz \end{aligned} \tag{7}$$

For a parallel connection the polarization direction is the same, therefore the $\bar{e}_{31}$ coefficient has the same sign for the top and bottom layers. The directions of $\bar{e}_{31}$ and $E_3(t)$ are expressed in Fig. 2, with black and redarrows separately.

The piezoelectric coupling term $\vartheta$ can be derived from Eq. (2), which is a function of time only. The internal moment in PZT layer is:

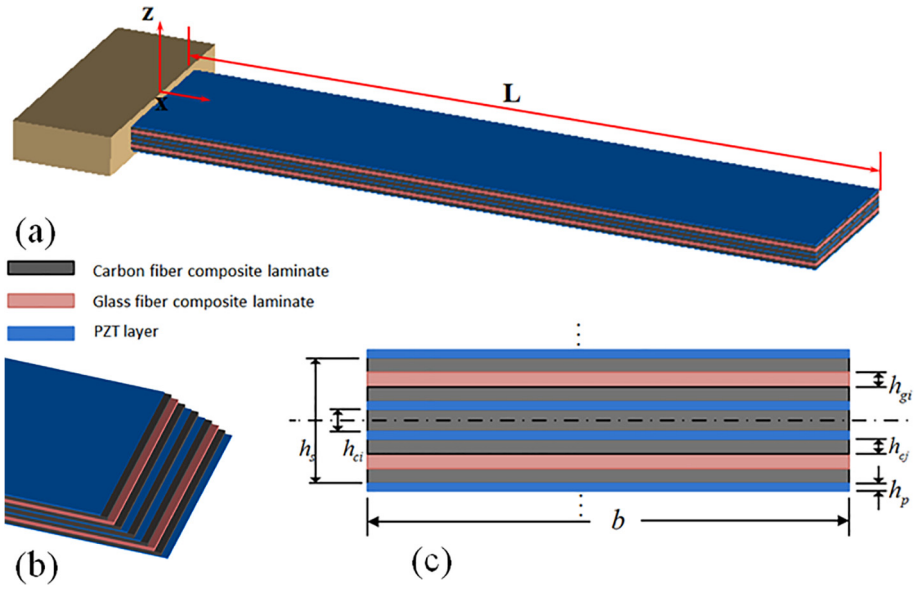


**Fig. 1.** Design of multi-layer piezoelectric energy harvester (MPEH). (a) Vibration cantilever beam with multi-layer composites laminates and PZT layers; (b) The internal design of the MPEH; (c) Cross section of a MPEH.

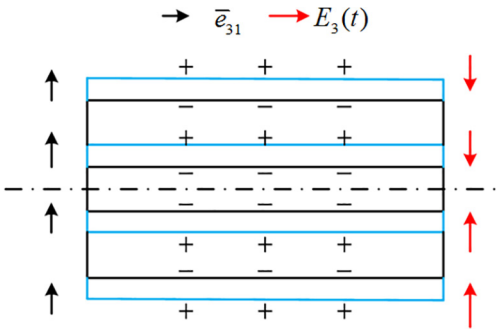


**Fig. 2.** Polarization direction and electrical field of parallel connection.

$$
\begin{aligned}
M_p(x,t) &= -b\left(\int_{\frac{h_{ci}}{2}}^{\frac{h_{ci}}{2}+h_p}\sigma_p z dz + \int_{-\frac{h_{c1}}{2}-h_p}^{-\frac{h_{ci}}{2}}\sigma_p z dz + \cdots + \int_{\frac{h_s}{2}}^{\frac{h_s}{2}+h_p}\sigma_p z dz \right.\\
&\quad \left. + \int_{-\frac{h_s}{2}-h_p}^{-\frac{h_s}{2}}\sigma_p z dz\right)\\
&= -b\left[\int_{\frac{h_{ci}}{2}}^{\frac{h_{ci}}{2}+h_p}(E_p\varepsilon_1^p(x,t)-\bar{e}_{31}E_3(t))z dz + \int_{-\frac{h_{ci}}{2}-h_p}^{-\frac{h_{ci}}{2}}(E_p\varepsilon_1^p(x,t)\right.\\
&\quad -\bar{e}_{31}E_3(t))z dz + \cdots + \int_{\frac{h_s}{2}}^{\frac{h_s}{2}+h_p}(E_p\varepsilon_1^p(x,t)-\bar{e}_{31}E_3(t))z dz\\
&\quad \left. + \int_{-\frac{h_s}{2}-h_p}^{-\frac{h_s}{2}}(E_p\varepsilon_1^p(x,t)-\bar{e}_{31}E_3(t))z dz\right]\\
&= M_p^*(x,t) - \frac{2b\bar{e}_{31}}{h_p}\left[v_p^i(t)\left(\left(\frac{h_{ci}}{2}+h_p\right)^2-\left(\frac{h_{ci}}{2}\right)^2\right)\right.\\
&\quad \left. + \cdots + v_p^j(t)\left(\left(\frac{h_s}{2}+h_p\right)^2-\left(\frac{h_s}{2}\right)^2\right)\right]\\
&= M_p^*(x,t) + \vartheta_p^i v_p^i(t) + \vartheta_p^{i+1}v_p^{i+1}(t) + \cdots + \vartheta_p^n v_p^n(t)
\end{aligned}
\tag{8}
$$

Substituting Eq. (6) into (1), the governing equation of the system can be obtained as:

$$
\begin{aligned}
&\frac{\partial^2}{\partial x^2}\left[YI\frac{\partial^2 w(x,t)}{\partial x^2}\right] + \frac{\partial^2}{\partial x^2}\left[c_s I\frac{\partial^3 w(x,t)}{\partial x^2\partial t}\right] + c_a\frac{\partial w(x,t)}{\partial t} + m\frac{\partial^2 w(x,t)}{\partial t^2}\\
&\quad + \vartheta_p^i v_p^i(t)[H(x)-H(x-L)] + \cdots + \vartheta_p^n v_p^n(t)[H(x)-H(x-L)]\\
&\quad = -(m+M_t)\frac{\partial^2 w_b(x,t)}{\partial t^2}
\end{aligned}
\tag{9}
$$

According to the linear piezoelectric materials constitutive equations, another essential governing equation is necessary to determine the unknown variables of $w(x,t)$ and $v_p$ as:

$$
D_3 = \bar{e}_{31}\varepsilon_1^p(x,t) + \varepsilon_{33}^S E_3 \tag{10}
$$

In Eq. (10), $D_3$ is the electrical displacement and $\varepsilon_{33}^S$ is the permittivity component at constant strain with the plane-stress assumption ($\varepsilon_{33}^S = \varepsilon_{33}^T - d_{31}^2 E_p$).

The electric current can be obtained by applying Guess' law [31]. Since the resistance across the inner and outer PZT layers is $R$, the total current can be expressed as:

$$
\frac{v_p^i}{R} + \cdots + \frac{v_p^n}{R} = \frac{d}{dt}\left(\int_A D_3\cdot\vec{n}\,dA\right) \tag{11}
$$

where $\vec{n}$ is the unit outward normal, and the integration is performed over the electrode area.

Since $\varepsilon_1^p(x,t) = -\bar{z}_p\frac{\partial^2 w(x,t)}{\partial x^2}$, by combining Eqs. (10) and (11) one obtains:

$$
\begin{cases}
\frac{v_p^i}{R} + \frac{bL\varepsilon_{33}^p}{h_p}\frac{dv^i(t)}{dt} = -\bar{e}_{31}b\bar{z}_p^i\int_o^L\frac{\partial^3 w(x,t)}{\partial x^2\partial t}dx\\
\vdots\\
\frac{v_p^n}{R} + \frac{bL\varepsilon_{33}^p}{h_p}\frac{dv^n(t)}{dt} = -\bar{e}_{31}b\bar{z}_p^n\int_o^L\frac{\partial^3 w(x,t)}{\partial x^2\partial t}dx
\end{cases}
\tag{12}
$$

where $\bar{z}_p$ is the distance between the centre of the PZT layers and the neutral axis. We can then solve Eqs. (9) and (12) by assuming the beam deflection with the modal expansion:

$$w(x,\ t) = \sum_{r=1}^{\infty} \phi_r(x)\eta_r(t) \tag{13}$$

where $\phi_r(x)$ is the mass normalized eigenfunction of the $r$th vibration mode and $\eta_r(t)$ is the modal participation factor. The mode $\phi_r(x)$ can be obtained by solving by undamped free vibration problem with clamped-free boundary conditions:

$$\phi_r(x) = C_1\cosh\lambda_r x + C_2\sinh\lambda_r x + C_3\cos\lambda_r x + C_4\sin\lambda_r x \tag{14}$$

where $C_i$ is an amplitude constant and $\lambda_r$ is the eigenvalue, which can be obtained from solving the characteristic equation with the BCs:

$$\begin{aligned} &\phi_r(0) = 0,\ \ \phi_r'(0) = 0 \\ &YI\phi_r''(L) = 0,\ \ YI\phi_r'''(L) = -\omega_r^2 M_t\phi_r(L) \end{aligned} \tag{15}$$

The eigenvalues $\lambda_r$ can be calculated from the classical transcendental equation:

$$\frac{\omega_r^2 M_t}{YI\lambda^3} = \frac{1 + \cosh\lambda L\cos\lambda L}{\cosh\lambda L\sin\lambda L - \sinh\lambda L\cos\lambda L} \tag{16}$$

The $r$th natural frequency can be therefore expressed as follows:

$$\omega_r = \lambda_r^2\sqrt{\frac{YI}{m}} \quad r = 1,\ 2,\ 3... \tag{17}$$

Eq. (16) can then be rewritten as follows:

$$\frac{M_t\lambda}{m}(\cosh\lambda L\sin\lambda L - \sinh\lambda L\cos\lambda L) - (1 + \cosh\lambda L\cos\lambda L) = 0 \tag{18}$$

The main vibration mode function can be therefore expressed as $\phi(x) = C_1(\cosh\lambda x - \cos\lambda x - A(\sinh\lambda x - \sin\lambda x))$.

According to Ref. [6], $A = \left(\frac{\sin\lambda L - \sinh\lambda L + \lambda\frac{M_t}{m}(\cos\lambda L - \cosh\lambda L)}{\cos\lambda L + \cosh\lambda L - \lambda\frac{M_t}{m}(\sin\lambda L - \sinh\lambda L)}\right)$.

The constant $C_1$ can be evaluated by applying the orthogonality conditions:

$$\begin{aligned} \int_0^L \phi_s(x)\frac{d^2}{dx^2}\left[YI\frac{d^2\phi_r(x)}{dx^2}\right]dx &= -\omega_r^2 M_t\phi_r(L)\phi_s(L) \\ &+ \int_0^L \frac{d^2\phi_s(x)}{dx^2}\left[YI\frac{d^2\phi_r(x)}{dx^2}\right]dx \\ \int_0^L YI\frac{d^2\phi_r(x)}{dx^2}\frac{d^2\phi_s(x)}{dx^2}dx &- \omega_r^2 M_t\phi_r(L)\phi_s(L) \\ &= \omega_r^2\int_0^L m\phi_r(x)\phi_s(x)dx \end{aligned} \tag{19}$$

when $r \neq s$:

$$0 = M_t\phi_r(L)\phi_s(L) + \int_0^L m\phi_r(x)\phi_s(x)dx,\ \ \int_0^L YI\frac{d^2\phi_r(x)}{dx^2}\frac{d^2\phi_s(x)}{dx^2}dx = 0.$$

In the case $r = s$: $M_t[\phi_r(L)]^2 + \int_0^L m[\phi_r(x)]^2dx = 1$, $\int_0^L YI\left[\frac{d^2\phi_r(x)}{dx^2}\right]^2dx = \omega_r^2$.

### 2.2. Output voltage and relative displacement

The equation of motion of the multi-layer PEH in modal coordinates can be obtained by substituting Eq. (13) into Eq. (9):

$$\frac{d^2\eta_r(t)}{dt^2} + 2\zeta_r\omega_r\frac{d\eta_r(t)}{dt} + \omega_r^2\eta_r(t) + \chi_r^i v^i(t) + \cdots + \chi_r^n v^n(t) = f_r(t) \tag{20}$$

In Eq. (20), the model electromechanical coupling term is:

$$\chi_r^i = \vartheta_p^i\frac{d\phi_r(x)}{dx}\bigg|_{x=L},\ \ i = 1{:}\ n \tag{21}$$

The model damping ratio is $\zeta_r$. The model force can be expressed as:

$$f_r(t) = -\left[\int_0^L \phi_r(x)mdx\right]\frac{d^2g(t)}{dt^2} - M_t\phi_r(L)\frac{d^2g(t)}{dt^2} \tag{22}$$

According to Kirchhoff laws, the relationship between the voltage and the current can be obtained as:

$$\begin{cases} C_p\frac{dv^i(t)}{dt} + \frac{v^i(t)}{2R} = i^i(t) \\ \quad\vdots \\ C_p\frac{dv^n(t)}{dt} + \frac{v^n(t)}{2R} = i^n(t) \end{cases} \tag{23}$$

If the PZT layers have all the same resistance, then Eq. (23) can be expressed as

$$C_p\frac{d[v^i(t) + v^n(t)]}{dt} + \frac{v^i(t) + v^n(t)}{2R} = i^i(t) + i^n(t) \tag{24}$$

where:

$$C_p = \frac{\varepsilon_{33}^S bL}{h_p},\ \ i^i(t) = \sum_{r=1}^{\infty}\kappa_r^i\frac{d\eta_r(t)}{dt},\ \ i^n(t) = \sum_{r=1}^{\infty}\kappa_r^n\frac{d\eta_r(t)}{dt}$$

The model coupling term is then:

$$\begin{aligned} \kappa_r^i &= -\frac{\bar{e}_{31}(h_{c1} + h_p)b}{2}\frac{d\phi_r(x)}{dx}\bigg|_{x=L} \\ &\vdots \\ \kappa_r^n &= -\frac{\bar{e}_{31}(h_s + h_p)b}{2}\frac{d\phi_r(x)}{dx}\bigg|_{x=L} \end{aligned} \tag{25}$$

The base excitation is assumed as a harmonic vibration around the z-direction:

$$\begin{aligned} g(t) &= Y_0e^{j\omega t} \\ f_r(t) &= F_re^{jwt} \end{aligned} \tag{26}$$

The model force $F_r$ can be given by Eqs. (26) and (22):

$$F_r = -m\omega^2Y_0\int_0^L \phi_r(x)dx - M_t\phi_r(L)Y_0\omega^2 \tag{27}$$

For the harmonic vibration case, the voltage and the model mechanical response are assumed to be harmonic at the same frequency:

$$\begin{aligned} \eta_r(t) &= H_re^{j\omega t} \\ v(t) &= Ve^{j\omega t} \end{aligned} \tag{28}$$

where the temporal term amplitude $H_r$ and $V$ are calculated by substituting Eqs. (27) and (28) into Eqs. (20) and (24).

$$\begin{cases} \left(\frac{1}{2R} + j\omega C_p\right)V^i - j\omega\sum_{r=1}^{\infty}\kappa_r^iH_r = 0 \\ \quad\vdots \\ \left(\frac{1}{2R} + j\omega C_p\right)V^n - j\omega\sum_{r=1}^{\infty}\kappa_r^nH_r = 0 \\ (-\omega^2 + j2\zeta_r\omega_r\omega + \omega_r^2)H_r + \chi_r^iV^i + \cdots + \chi_r^nV^n = F_r \end{cases} \tag{29}$$

From Eq. (29), one can obtain $H_r$ and $V^i$, and then substitute in Eq. (28) to express the voltage output of the system:

$$v^i(t) = \frac{\sum_{r=1}^{\infty}\frac{j\omega\kappa_r^iF_r}{j2\zeta_r\omega_r\omega - \omega^2 + \omega_r^2}}{\frac{1}{2R} + j\omega C_p + \sum_{r=1}^{\infty}\frac{j\omega(\kappa_r^i\chi^i + \cdots + \kappa_r^n\chi^n)}{j2\zeta_r\omega_r\omega - \omega^2 + \omega_r^2}}e^{j\omega t} \tag{30}$$

An important point to be drawn from observing Eq. (30) is that the effect of the embedded additional PZT layers does not consist only in add another PEH with a parallel connection; the voltage output of the

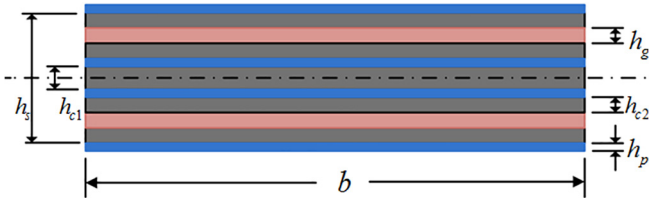


**Fig. 3.** Cross-section of MPEH with 4 PZT layers.

inner and outer part of the beam has also a coupling influence.

The steady state mechanical response of the multi-layer PEH can be given as follows:

$$\eta_r(t) = \frac{F_r}{j2\zeta_r\omega_r\omega - \omega^2 + \omega_r^2 + \frac{\sum_{r=1}^{\infty} j\omega(\kappa_r^i\chi^i + \cdots + \kappa_r^n\chi^n)}{\frac{1}{2R} + j\omega C_p}} e^{j\omega t} \tag{31}$$

The displacement at point x is therefore:

$$w(x,t) = \sum_{r=1}^{\infty} \frac{F_r\phi_r(x)}{j2\zeta_r\omega_r\omega - \omega^2 + \omega_r^2 + \frac{\sum_{r=1}^{\infty} j\omega(\kappa_r^i\chi^i + \cdots + \kappa_r^n\chi^n)}{\frac{1}{2R} + j\omega C_p}} e^{j\omega t} \tag{32}$$

Furthermore, the total power output provided by the multi-layer PEH is:

$$P(t) = \left[ \left( \frac{\sum_{r=1}^{\infty} \frac{j\omega\kappa_r^i F_r}{j2\zeta_r\omega_r\omega - \omega^2 + \omega_r^2}}{\frac{1}{2R} + j\omega C_p + \sum_{r=1}^{\infty} \frac{j\omega(\kappa_r^i\chi^i + \cdots + \kappa_r^n\chi^n)}{j2\zeta_r\omega_r\omega - \omega^2 + \omega_r^2}} e^{j\omega t} \right)^2 + \cdots + \left( \frac{\sum_{r=1}^{\infty} \frac{j\omega\kappa_r^n F_r}{j2\zeta_r\omega_r\omega - \omega^2 + \omega_r^2}}{\frac{1}{2R} + j\omega C_p + \sum_{r=1}^{\infty} \frac{j\omega(\kappa_r^i\chi^i + \cdots + \kappa_r^n\chi^n)}{j2\zeta_r\omega_r\omega - \omega^2 + \omega_r^2}} e^{j\omega t} \right)^2 \right] \Big/ R \tag{33}$$

### 2.3. MPEH with 4 PZT layers

From the model presented in Sections 2.1 and 2.2, one can calculate the fundamental natural frequency and the voltage output of MPEH. If the MPEH has four PZT layers (Fig. 3), then the model equations can be further simplified.

In that case, the flexural rigidity of the piezoelectric elastic composites of Eq. (7) can be expressed as:

$$\begin{aligned} YI &= b\sum_{k=1}^{N_c} (\overline{Q}_{11})_k^c \int_{z_{k-1}}^{z_k} z^2 dz + b\sum_{k=1}^{N_g} (\overline{Q}_{11})_k^g \int_{z_{k-1}}^{z_k} z^2 dz + E_p b\sum_{i=1}^{N_p} \int_{z_{k-1}}^{z_k} z^2 dz \\ &= b\left[ \sum_{k=1}^{N_c} (\overline{Q}_{11})_k^c \int_{z_{k-1}}^{z_k} z^2 dz + \sum_{k=1}^{N_g} (\overline{Q}_{11})_k^g \int_{z_{k-1}}^{z_k} z^2 dz \right. \\ &\quad \left. + \frac{2E_p}{3}\left( \left(\frac{h_{c1}}{2} + h_p\right)^3 - \left(\frac{h_{c1}}{2}\right)^3 + \left(\frac{h_s}{2} + h_p\right)^3 - \left(\frac{h_s}{2}\right)^3 \right) \right] \end{aligned} \tag{34}$$

The internal bending moment exist in the PZT layer can be obtained from Eq. (8):

$$\begin{aligned} M_p(x,t) &= -b\left( \int_{\frac{h_{c1}}{2}}^{\frac{h_{c1}}{2}+h_p} \sigma_p z dz + \int_{\frac{h_s}{2}}^{\frac{h_s}{2}+h_p} \sigma_p z dz + \int_{-\frac{h_{c1}}{2}-h_p}^{-\frac{h_{c1}}{2}} \sigma_p z dz \right. \\ &\quad \left. + \int_{-\frac{h_s}{2}-h_p}^{-\frac{h_s}{2}} \sigma_p z dz \right) \\ &= -b\left[ \int_{\frac{h_{c1}}{2}}^{\frac{h_{c1}}{2}+h_p} E_p\varepsilon_1^p(x,t) z dz + \int_{\frac{h_s}{2}}^{\frac{h_s}{2}+h_p} E_p\varepsilon_1^p(x,t) z dz \right. \\ &\quad + \int_{-\frac{h_{c1}}{2}-h_p}^{-\frac{h_{c1}}{2}} E_p\varepsilon_1^p(x,t) z dz + \int_{-\frac{h_s}{2}-h_p}^{-\frac{h_s}{2}} E_p\varepsilon_1^p(x,t) z dz \\ &\quad + \int_{\frac{h_{c1}}{2}}^{\frac{h_{c1}}{2}+h_p} \bar{e}_{31}\frac{v_p^{in}(t)}{h_p} z dz + \int_{\frac{h_s}{2}}^{\frac{h_s}{2}+h_p} \bar{e}_{31}\frac{v_p^{out}(t)}{h_p} z dz \\ &\quad \left. + \int_{-\frac{h_{c1}}{2}-h_p}^{-\frac{h_{c1}}{2}} -\bar{e}_{31}\frac{v_p^{in}(t)}{h_p} z dz + \int_{-\frac{h_s}{2}-h_p}^{-\frac{h_s}{2}} -\bar{e}_{31}\frac{v_p^{out}(t)}{h_p} z dz \right] = M_p^*(x,t) \\ &\quad -b\left[ \bar{e}_{31}\frac{v_p^{in}(t)}{h_p} z^2 \Big|_{\frac{h_{c1}}{2}}^{\frac{h_{c1}}{2}+h_p} + \bar{e}_{31}\frac{v_p^{out}(t)}{h_p} z^2 \Big|_{\frac{h_s}{2}}^{\frac{h_s}{2}+h_p} - \bar{e}_{31}\frac{v_p^{in}(t)}{h_p} z^2 \Big|_{-\frac{h_{c1}}{2}-h_p}^{-\frac{h_{c1}}{2}} \right. \\ &\quad \left. - \bar{e}_{31}\frac{v_p^{out}(t)}{h_p} z^2 \Big|_{-\frac{h_s}{2}-h_p}^{-\frac{h_s}{2}} \right] = M_p^*(x,t) \\ &\quad -b\bar{e}_{31}\left[ \frac{v_p^{in}(t)}{h_p}\left( \left(\frac{h_{c1}}{2} + h_p\right)^2 - \left(\frac{h_{c1}}{2}\right)^2 \right) - \frac{v_p^{in}(t)}{h_p}\left( \left(\frac{h_{c1}}{2}\right)^2 - \left(\frac{h_{c1}}{2} + h_p\right)^2 \right) \right. \\ &\quad \left. + \frac{v_p^{out}(t)}{h_p}\left( \left(\frac{h_s}{2} + h_p\right)^2 - \left(\frac{h_s}{2}\right)^2 \right) - \frac{v_p^{out}(t)}{h_p}\left( \left(\frac{h_s}{2}\right)^2 - \left(\frac{h_s}{2} + h_p\right)^2 \right) \right] \\ &= M_p^*(x,t) - \frac{2b\bar{e}_{31}}{h_p}\left[ v_p^{in}(t)\left( \left(\frac{h_{c1}}{2} + h_p\right)^2 - \left(\frac{h_{c1}}{2}\right)^2 \right) \right. \\ &\quad \left. + v_p^{out}(t)\left( \left(\frac{h_s}{2} + h_p\right)^2 - \left(\frac{h_s}{2}\right)^2 \right) \right] = M_p^*(x,t) + \vartheta_p^{in} v_p^{in}(t) + \vartheta_p^{out} v_p^{out}(t) \end{aligned} \tag{35}$$

In Eq. (35), $M_p^*(x,t)$ is the internal moment induced by the elastic part of the PZT layer, $\vartheta_p^{in}$ is the piezoelectric coupling term of two inner PZTs and $\vartheta_p^{out}$ is the piezoelectric coupling term of two outer PZT layers. The output voltage of the inner and outer PZT layers are $v_p^{in}$ and $v_p^{out}$.

## 3. Experimental setup

The hybrid MPEH fabricated consists of carbon fibre laminates (SE70 CFRP, Gurit Ltd), glass fibre composites (SE70 E-Glass, Gurit, Ltd) and PZT (Sinoceramics Inc., Shanghai, China) layers. The low curing temperature of the prepreg (70 °C) is significantly lower than the Curie one of the PZT. The properties of prepregs are listed in Table 1. The plies are sized by using a cutting machine (Genesis 2100, BLACK & WHITE Ltd), then laid up with a $[PZT/0_c/90_c/0_g/0_c/90_c/PZT/90_c]_S$ stacking sequence. Here the subscript c indicates the CFRP, and g stands for the E-glass layer. The PZT layers are placed inside the hybrid composites plies before curing. The resin inside the prepregs also acts as adhesive for the PZT layers. The curing progress is performed in an oven at 70 °C, under a pressure of 1 bar for 16 h. Here, the pressure is controlled by a vacuum pump which connected with the vacuum-bagged specimen. After curing the plate was cut into a 10 mm width and 95 mm length. The dimensions of the PZT layers connected in parallel are 10 mm × 80 mm × 0.2 mm. Copper foils are placed on the free surfaces of the PZTs, and connected with copper wires as electrodes. The tip mass fixed at the free end is a steel rectangular block of 10 mm × 10 mm × 15 mm (11.7 g).

To validate the electro-mechanical model, the fundamental natural frequency and the power generation ability of the MPEH are firstly tested. The experimental setup is shown in Fig. 4. The MPEH sample is

**Table 1**
Parameters of materials.

| Properties | | SE70 CFRP | SE70 E-Glass | PZT-5H |
|---|---|---|---|---|
| Density [kg/m$^3$] | $\rho$ | 1502 | 1936 | 7500 |
| Thickness [mm] | $t$ | 0.2 | 0.2 | 0.2 |
| Moduli [GPa] | $E_1$ | 130.33 | 40.74 | 61 |
| | $E_2$ | 7.22 | 10.1 | 61 |
| | $E_3$ | – | – | 48 |
| | $G_{12}$ | 4.23 | 3.82 | 23 |
| | $G_{13}$ | – | – | 23 |
| | $G_{23}$ | – | – | 23.5 |
| Poisson's ratios | $v_{12}$ | 0.337 | 0.255 | 0.289 |
| | $v_{13}$ | – | – | 0.512 |
| | $v_{23}$ | – | – | 0.408 |
| Piezoelectric strain constants [$\times 10^{-12}$ m/V] | $d_{31}$, $d_{32}$ | – | – | -270 |
| | $d_{33}$ | – | – | 550 |
| Dielectric property [$\times 10^{-8}$ F/m] | $D_{11}$ | – | – | 1.505 |
| | $D_{22}$ | – | – | 1.505 |
| | $D_{33}$ | – | – | 1.301 |

held by two thick acrylic plates and mounted on the top of a shaker (LDS shaker system), which is controlled by a NI USB-6221 multi-functional I/O board (National Instrument) and power amplifier (LDS PA25E Shaker Power Amplifier). The sensors are an accelerometer (PCB 333M07) and single point laser vibrometer (Ometron VPI 8330). The signal of the time domain velocity has been then FFT-transformed, with a sampling frequency of 2048 Hz and sampling time of 3 s. The signal has been subjected to a Hanning window to reduce the spectral leakage. The accelerometer is fixed to the clamped side of the beam to monitor the vibration of shaker, and the laser vibrometer measures the velocity of the tip mass.

The natural frequency is firstly measured by using an impact hummer (force transducer PCB 086D05) while the MPEH is fixed at the clamp. The output of the force transducer and the laser vibrometer is generated through the NI USB-6221 from a signal coupler (Kistler 5134).

To measure the power generation performance, the MPEH is fixed to the shaker as a clamped-free beam. The multifunction I/O device generates a sinusoidal waveform to the power amplifier. The amplitude of the vibration acceleration is regulated through the amplifier ratio, and the power generation is measured at different acceleration levels. The output voltage is measured by an oscilloscope (PicoScope 2204A) with two channels. Two channels measure the voltage of two inner PZT layers and the outer two PZT layers, respectively.

**Table 2**
Natural frequency.

| | Natural Frequency | Error |
|---|---|---|
| Theoretical model | 92.6 Hz | 0.76% |
| FEA | 91.07 Hz | 0.9% |
| Experimental test | 91.9 Hz | – |

The theoretical electromechanical model presented above has been coded in a Matlab platform. The frequencies used in both the experimental and numerical model range between 50 Hz and 115 Hz during the output voltage test at 10 kΩ resistance. Several different excitation accelerations (0.5 g, 1 g, 2 g, 3 g) are chosen to discuss the performance of the MPEH. The output power is calculated based on the experimental data under different resistance loads as $P = V^2/R$.

For further benchmarking, a finite element (FE) model is also developed using the commercial code ABAQUS. The composite laminates are represented by solid laminate elements (C3D8R), while the PZT layers are simulated by using piezoelectric element C3D8E (8-node linear piezoelectric brick). The FEA mesh discretization is represented by squares with 2.5 mm side for the composites beam, and bricks with 2.5 mm side for the PZT transducers. The surfaces of the PZTs are bonded to the surfaces of the composites beam by 'tie' constraint during the assembly. The FEA eigensolver is a Lanczos one.

## 4. Results and discussions

### 4.1. Fundamental frequency of the MPEH

The results of the natural frequency associated to the first mode are shown in Table 2. The experimental result is 91.9 Hz, with an average modal damping ratio calculated from three FRFs as $\zeta = 0.018$. The theoretical model provides a 92.6 Hz natural frequency. The finite element analysis result (91.07 Hz) is also close to the experimental test data.

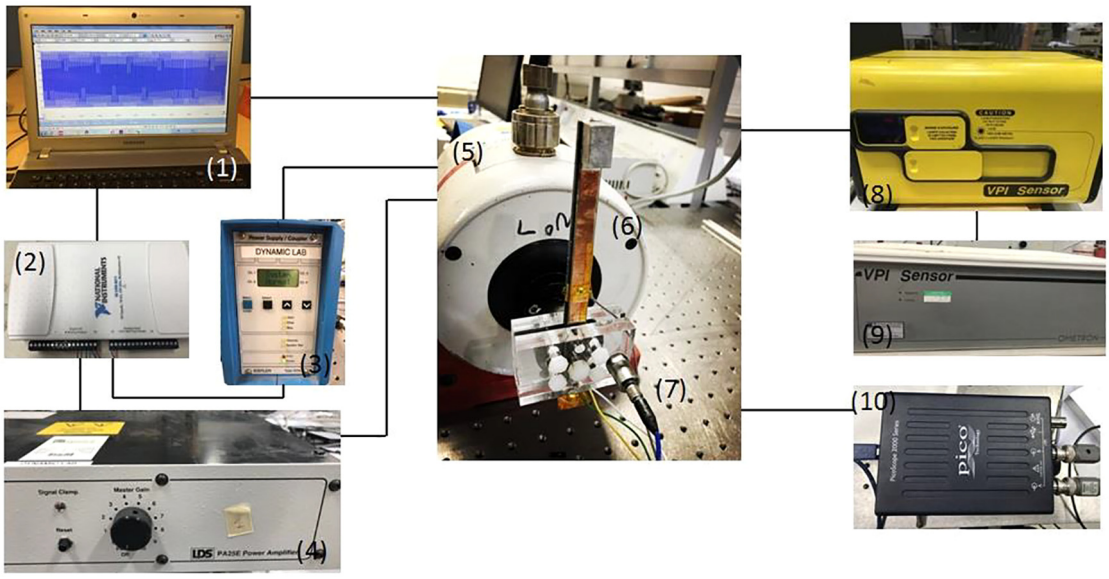


**Fig. 4.** Experimental setup for the vibration test of the MPEH system. (1) Computer for data logging and control; (2) NI USB-6211 multifunction I/O device; (3) Kistler 5134 power supply/coupler; (4) Ling Dynamic Systems LDS PA25E Shaker Power Amplifier; (5) Electrodynamic shaker; (6) MPEH with tip mass; (7) Acceleration transducer; (8) Ometron scanning laser Doppler vibrometer 8330; (9) Vibrometer controller; (10) PicoScope 2004A oscilloscope.

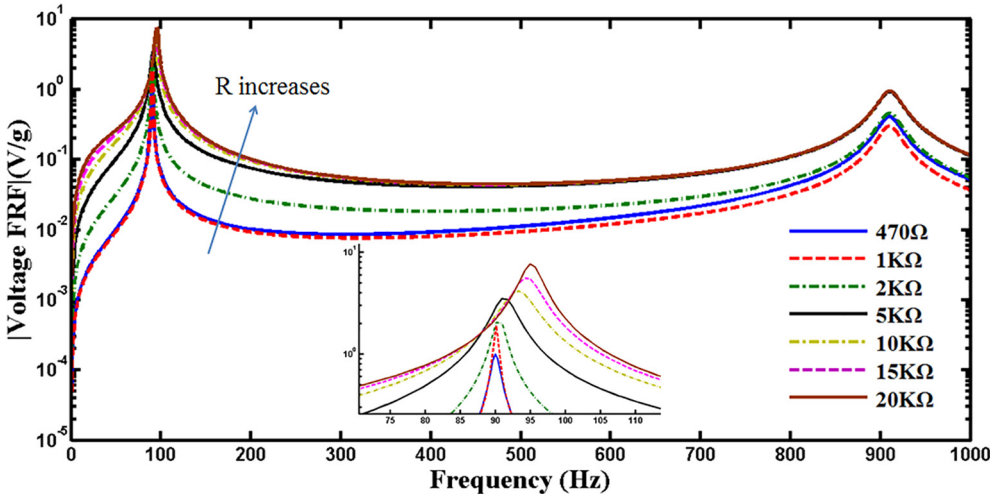


**Fig. 5.** Voltage FRF theoretical simulation for the MPEH.

**Table 3**
Comparisons between maximum voltage FRFs of the MPEH and the PEH.

| Resistance | MPEH | | PEH | |
|---|---|---|---|---|
| | Maximum voltage FRF (V/g) | Corresponding frequency (Hz) | Maximum voltage FRF (V/g) | Corresponding frequency (Hz) |
| 470 Ω | 1.003 | 89.97 | 0.37 | 98.09 |
| 1 kΩ | 1.91 | 90.13 | 0.65 | 98.09 |
| 2 kΩ | 2.05 | 90.13 | 0.91 | 98.21 |
| 5 kΩ | 3.52 | 90.92 | 1.40 | 99.68 |
| 10 kΩ | 4.17 | 93.31 | 1.92 | 100.5 |
| 15 kΩ | 5.58 | 94.11 | 2.66 | 101.3 |
| 20 kΩ | 6.50 | 94.9 | 3.38 | 102.9 |

### 4.2. Simulation results of voltage response

The simulation results of MPEH with different resistance loads are shown in Fig. 5. The maximum voltage FRF value is close near the natural frequency, with the voltage getting larger with the increase of resistance R. In this case the load resistances are increased from 470Ω to $20K\Omega$, and the peak values of the first mode are listed in Table 3. The voltage FRF amplitude at 470 Ω is 1.003 V/g, while at 20 kΩ the voltage FRF increases to 7.7 V/g. The corresponding frequency of the peak value shifts with different load resistances. For small Rs (470 Ω), the resonance frequency is 89.9 Hz, which increases slowly to 90.9 Hz at R= 5 kΩ. After that point the resonance frequency visibly increases to 93.3 Hz at R= 10 kΩ, then the increase is less significant (94.9 Hz at 20 kΩ). The same type of behavior is also observed by Rafique et al. in the case of bimorph cantilever energy harvesters [23].

We have made a comparison between the proposed MPEH design and a traditional PEH with only two PZT layers on the external surfaces. Firstly, both the MPEH and the PEH have the same length, width, thickness, tip mass and materials. The layup of PEH is the following: $[PZT/0_c/90_c/0_g/0_c/90_c/0_c/90_c]_S$. The stacking sequences difference between the MPEH and PEH only exists in the second ply, the inner PZT layers of the MPEH are replaced by 0 degree CFRP plies. The flexural stiffness of composites beam can be calculated by the follow equation:

$$D_{11} = \sum_{k=1}^{N} (\overline{Q}_{11})_K \left( t_k \overline{z}_k^2 + \frac{t_k^3}{12} \right), \quad \overline{z}_k = \frac{1}{2}(z_k + z_{k-1}) \tag{36}$$

Here $\overline{Q}_{11}$ is defined in Eq. (4). The flexural stiffness of the MPEH and PEH with 0.2 mm thickness PZT can be calculated: $D_{11,MPEH} = 223$ N/m, $D_{11,PEH} = 225$ N/m. We can find that the flexural stiffness of the MPEH and the PEH are almost the same, the error is only 0.9%.

Fig. 6 shows the comparison of the voltage FRFs between the MPEH and the PEH with two different load resistances. One can observe that the resonant frequencies of the PEH are higher than the ones of the MPEH. The MPEH amplitude of the voltage response is however significantly improved compared to the PEH case (Table 3). For a resistance of 5 kΩ, the voltage FRF of the MPEH reaches 3.52 V/g at 90.9 Hz, while the PEH can only generate 1.4 V/g at 99.7 Hz. For each load resistances used, the maximum voltage generated by the MPEH on average is about 2.2 times higher than the PEH.

We also consider the case in which the thickness of the PZT layers used in the PEH is increased to 0.4 mm, which means that the total volume of the PZTs for the PEH and the MPEH is the same. In that case, if all the PZT layers are located on the external surfaces of the composites beam, the flexural stiffness $D_{11}$ term will become larger than the one of the MPEH configuration. The resonance frequency of the PEH would be significantly higher than the MPEH one, and the power generated by the PEH would be smaller than the MPEH case (Fig. 7). The MPEH and the PEH with 0.4 mm thickness PZTs are calculated

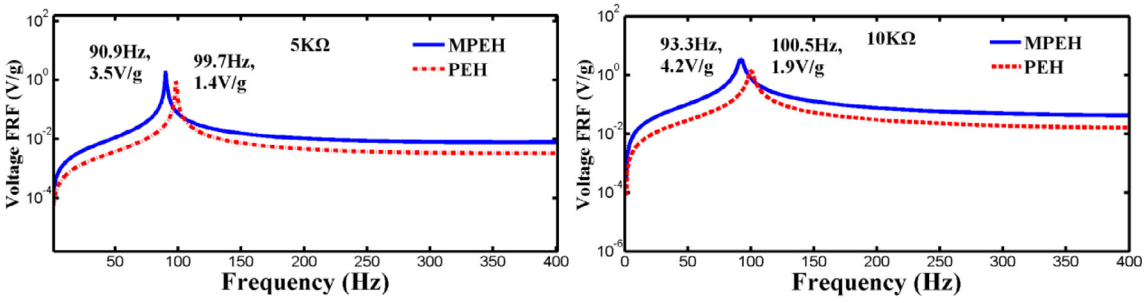


**Fig. 6.** Comparisons of the voltage FRF between the MPEH and the PEH.

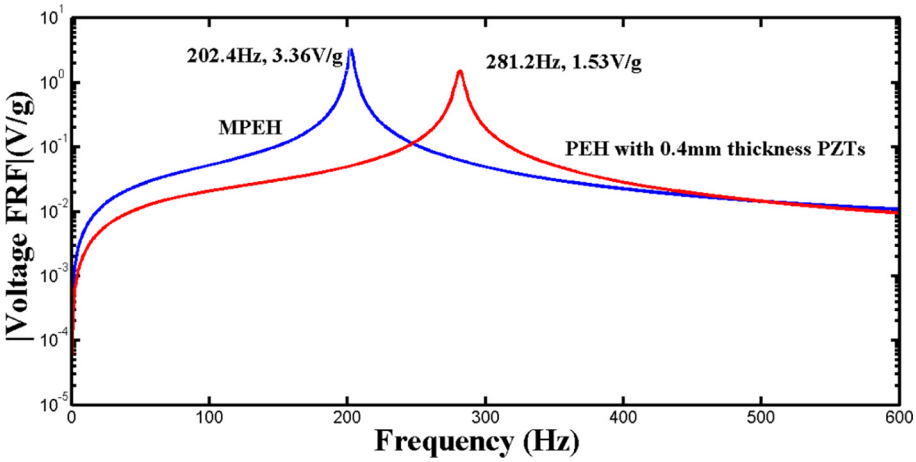


**Fig. 7.** Voltage FRF comparisons between the MPEH and the PEH (0.4 mm thickness PZT).

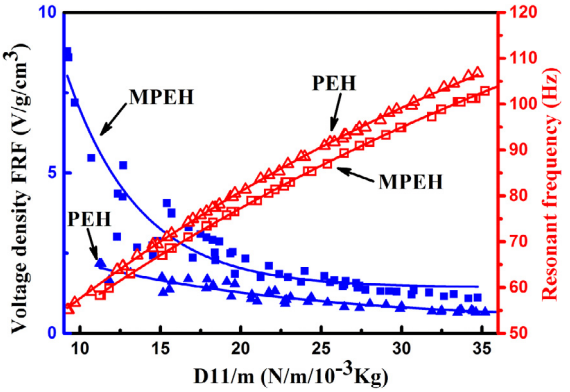


**Fig. 8.** Peak voltages density FRFs and resonant frequencies versus the specific flexural stiffness $D_{11}/m$ for the MPEHs and the PEHs.

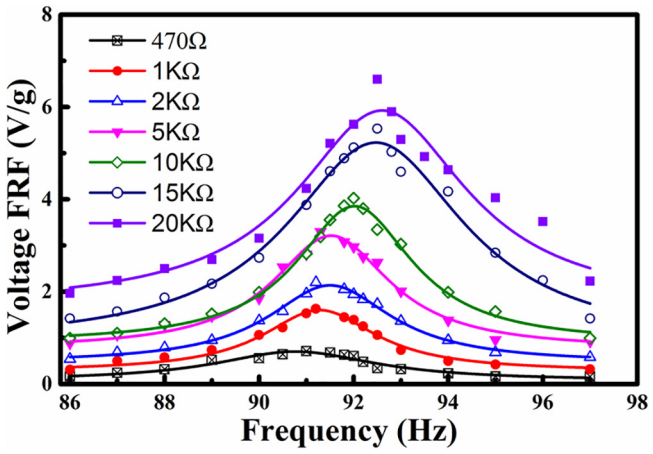


**Fig. 10.** Experimental voltage responses of MPEH at seven difference loads.

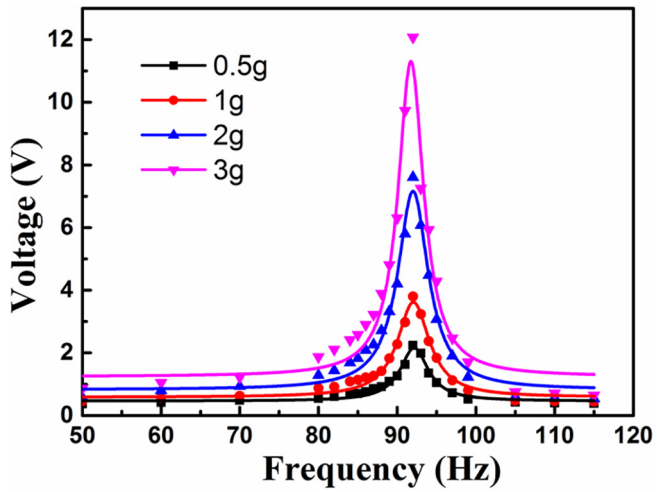


**Fig. 9.** Experimental RMS voltages with 10 kΩ load resistance of the MPEH.

without tip mass.

A more comprehensive comparison between the MPEH and PEH configurations (all based on using 0.2 mm thickness PZTs) is by considering their resonant frequencies and voltage density FRFs versus the specific flexural stiffness ($D_{11}/m$, where $m$ is the mass of the composite beams). The stacking sequences of the beams are changed to obtain different flexural stiffness $D_{11}$. The volumes of the beams for all the stacking sequences are kept the same ($8 \times 1 \times 0.32$ cm$^3$), as well as the modal damping ratio, for simplicity. As shown in Fig. 8, the peak voltage density FRF decreases with the increase of the specific flexural stiffness, but the values provided by the MPEHs are always larger than the ones provided by the PEHs. This is particularly valid for low specific flexural stiffness ($D_{11}/m$ less than $15e^{-3}$ N/m/kg). These results are quite important, because they show that by using MPEHs with comparable more compliant stacking sequences, the output voltage density is significantly enhanced compared a PEH configuration. The difference in terms of resonant frequencies between MPEHs and PEHs is however less marked, and the two configurations show a very similar sensitivity trend versus the specific flexural stiffness.

### 4.3. Experimental validation

Fig. 9 shows the experimental results related to the multi-layer piezoelectric energy harvester with a 10 kΩ load resistance under four different base accelerations. The maximum RMS voltage occurs at 92 Hz. The analogous peak in the theoretical model is 93.3 Hz. For an excitation of 0.5 g the RMS voltage of the MPEH is 2.24 V; with the increase of the excitation level, the voltage generated by the MPEH reaches 3.79 V at 1 g, 7.61 V at 2 g and 12.07 V at 3 g. The average maximum experimental voltage FRF is 4.02 V/g, which is close to the theoretical result of the MPEH with the same load resistance (4.17 V/g). The average error between the experimental data and the simulation results at 10 kΩ is 3.57%.

The sensitivity of the MPEH performance versus different load resistance values is shown in Fig. 10. The voltage FRF at 470 Ω is 0.71 V/g and occurs at 91 Hz. The analogous theoretical result is 1.003 V/g at 89.97 Hz. The frequency slowly increases to 91.3 Hz at 5 kΩ. When the

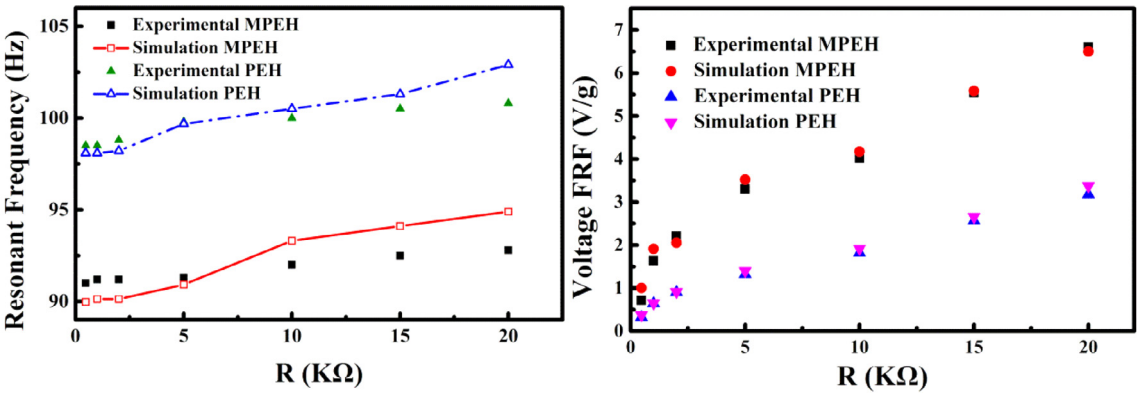


**Fig. 11.** Comparisons between experimental and theoretical resonance and voltage results of the MPEH and PEH configurations.

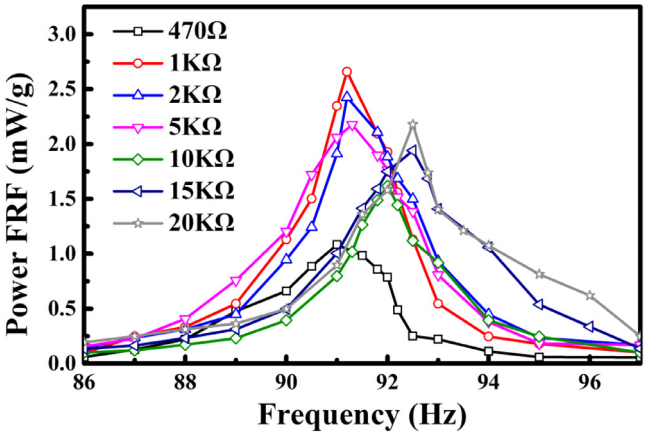


**Fig. 12.** Experimental power FRFs of the MPEH.

load resistance is 20 kΩ the resonance frequency moves to 92.5 Hz. In the range between 470 Ω and 20 kΩ, the experimental results show a general good agreement with the ones provided by the model developed in this work. The output voltage of the MPEH becomes larger with the increasing load resistance, and the resonance frequency of the maximum voltage FRF also shift towards higher values.

Fig. 11 features a comparison between experimental and simulated resonance frequencies and voltage FRFs related to MPEHs and PEHs. In this case, the resonance frequency corresponds to the frequency at which the magnitude of the FRF is the largest. The PEH considered in this part is fabricated with the same materials used for the MPEH, and the stacking sequence is $[PZT/0_c/90_c/0_g/0_c/90_c/0_c/90_c]_S$. Both the simulations and the experimental data show that the resonance frequencies for the two types of energy harvester increase with the load resistances. The maximum percentage error between experimental and theoretical resonance frequencies is 2.52%. For a given resistance, the MPEH can generate more voltage than the PEH configuration. At 5 kΩ the MPEH can produce a 2.5 times higher voltage FRF peak than the PEH, and at 20 kΩ resistance the MPEH can generate again about 1.98 times more voltage than the PEH system. Fig. 11 also shows that the theoretical model can reproduce the response of the MPEH system in a very adequate fashion.

The output power FRFs of the MPEH is shown in Fig. 12. The maximum power for a given load resistance occurs at the same resonance frequencies illustrated in Fig. 10. With lower resistances (less than 10 kΩ), the maximum amplitude has peak at 1 kΩ (2.66 mW/g), after which the power decreases with the increase of the resistance (1.62 mW/g at 10 kΩ). For increasing loads (15 kΩ or 20 kΩ), the power response shows a gradual increase to 2.18 mW/g.

## 5. Conclusions

In this paper, a new design of piezoelectric energy harvesting system with multiple composite laminates and PZT layers is presented. The electromechanical model of the MPEH is developed based on Euler-Bernoulli beam theory. The structure of the MPEH consists of carbon fibre and glass fibre laminates, and PZT layers. The elastic properties of the beams are defined by using classical laminate theory, and the effect given by the parallel connection of PZT layers is also taken into account. The model can reproduce the fundamental frequencies of the MPEH system and the voltage response with different load resistances. The results from the simulations show that the MPEH voltage FRF is maximized when the excitation frequency is close to the one associated to the first mode of the MPEH. The resonance frequency of the maximum voltage output changes with the load resistances, which indicates that an increase of the load resistances makes the resonance frequency larger. Both the experimental and the simulation results give evidence that the voltage FRFs of the MPEH increases with larger load resistances, and the modal provides a very good comparison with the test data. The comparison between the MPEH and a classical PEH configuration shows that the MPEH can provide an output voltage between 1.98 and 2.5 times higher of the PEH system with the same load resistance. It is therefore apparent that multi-layer piezoelectric energy harvesting designs can generate more power compared to traditional ones. MPEHs can therefore be considered for further concepts, like the modification of MEMS PEH, or nonlinear vibration applications currently covered by PEH designs.

## Acknowledgements

QL acknowledges the support of the National Natural Science Foundation of China (Grant Nos.: 11632005, 11672086, 11421091) and China Scholarship Council. FS is grateful to the logistic support from the MSCA ITN VIPER program regarding the use of the software and the access to the Material Laboratory of the Faculty of Engineering. QL and FS are also grateful for the access to BLADE (Bristol Laboratory of Dynamics Engineering) of the University of Bristol for the dynamics tests.

## References

[1] Kim HS, Kim J-H, Kim J. A review of piezoelectric energy harvesting based on vibration. Int J Precis Eng Manuf 2011;12:1129–41.
[2] Williams CB, Yates RB. Analysis of a micro-electric generator for micro systems. Sens Actuators A 1996;52:8–11.
[3] Wang Q-M, Cross LE. Constitutive equations of symmetrical triple layer piezoelectric benders. IEEE Trans Ultrason Ferroelectr Freq Control 1999;46:1343–51.
[4] Erturk A, Inman DJ. On mechanical modeling of cantilevered piezoelectric vibration energy harvesters. J Intell Mater Syst Struct 2008;19:1311–25.
[5] Erturk A, Inman DJ. A distributed parameter electromechanical model for cantilevered piezoelectric energy harvesters. ASME J Vib Acoust 2008;130:041002.

[6] Erturk A, Inman DJ. An experimentally validated bimorph cantilever model for piezoelectric energy harvesting from base excitations. Smart Mater Struct 2009;18:025009.
[7] Song HJ, Choi YT, Wereley NM, Purekar AS. Energy harvesting devices using macro-fiber composite materials. J Intell Mater Syst Struct 2010;21:647–58.
[8] Erturk A, Hoffman J, Inman DJ. A piezomagnetoelastic structure for broadband vibration energy harvesting. Appl Phys Lett 2009;94:254102.
[9] Erturk A, Inman DJ. Broadband piezoelectric power generation on high-energy orbits of the bistable Duffing oscillator with electromechanical coupling. J Sound Vib 2011;330:2339–53.
[10] Litak G, Friswell MI, Adhikari S. Magnetopiezoelastic energy harvesting driven by random excitations. Appl Phys Lett 2010;94:214103.
[11] Ali SF, Adhikari S, Friswell MI, Narayanan S. The analysis of piezomagnetoelastic energy harvesters under broadband random excitations. J Appl Phys 2011;109:074904.
[12] Ferrari M, Bau M, Guizzetti M, Ferrari V. A single-magnet nonlinear piezoelectric converter for enhanced energy harvesting from random vibrations. Sens Actuators A 2011;172:287–92.
[13] Friswell MI, Ali SF, Bilgen O, Adhikari S, Lees AW, Litak G. Non-linear piezoelectric vibration energy harvesting from a vertical cantilever beam with tip mass. J Intell Mater Syst Struct 2012;23:1505–21.
[14] Tang L, Yang Y, Soh CK. Improving functionality of vibration energy harvesters using magnets. J Intell Mater Syst Struct 2012;23:1433–49.
[15] Zhou S, Cao J, Inman DJ, Lin J, Liu S, Wang Z. Broadband tristable energy harvester: modeling and experiment verification. Appl Energy 2014;133:33–9.
[16] Abdelkefi A, Barsallo N. Nonlinear analysis and power improvement of broadband low-frequency piezomagnetoelastic energy harvesters. Nonlinear Dyn 2016;83:41–56.
[17] Twiefel J, Westermann H. Survey on broadband techniques for vibration energy harvesting. J Intell Mater Syst Struct 2013;24:1291–302.
[18] Betts DN, Kim HA, Bowen CR, Inman DJ. Static and dynamic analysis of bistable piezoelectric-composite plates for energy harvesting. 53rd AIAA/ASME/ASCE/AHS/ASC Struct. Struct. Dyn. Mater. Conf. 2012. 2012.
[19] Arrieta AF, Delpero T, Bergamini AE, Ermanni P. Broadband vibration energy harvesting based on cantilevered piezoelectric bi-stable composites. Appl Phys Lett 2013;102:173904.
[20] Pan D, Dai F, Li H. Piezoelectric energy harvester based on bi-stable hybrid symmetric laminate. Compos Sci Technol 2015;119:34–45.
[21] Pan D, Li Y, Dai F. The influence of lay-up design on the performance of bi-stable piezoelectric energy harvester. Compos Struct 2017;161:227–36.
[22] Qi S, Shuttleworth R, Olutunde OS, Wright J. Design of a multiresonant beam for broadband piezoelectric energy harvesting. Smart Mater Struct 2010;19:094009.
[23] Rafique S, Bonello P. Experimental validation of a distributed parameter piezoelectric bimorph cantilever energy harvester. Smart Mater Struct 2010;19:094008.
[24] Adhikari S, Friswell MI, Inman DJ. Piezoelectric energy harvesting from broadband random vibrations. Smart Mater Struct 2009;18:115005.
[25] Paknejad A, Rahimi G, Farrokhabadi A, Khatibi MM. Analytical solution of piezoelectric energy harvester patch for various thin multilayer composite beams. Compos Struct 2016;154:694–706.
[26] Akbar M, Curiel-Sosa JL. Piezoelectric energy harvester composite under dynamic bending with implementation to aircraft wingbox structure. Compos Struct 2016;153:193–203.
[27] Erturk A, Renno JM, Inman DJ. Modeling of piezoelectric energy harvesting from an L-shaped beam-mass structure with an application to UAVs. J Intell Mater Syst Struct 2009;20:529–44.
[28] El-Hebearya MMR, Arafab MH, Megahed SM. Modeling and experimental verification of multi-modal vibration energy harvesting from plate structures. Sens Actuators A 2013;193:35–47.
[29] Li HT, Yang Z, Zu J, Qin WY. Numerical and experimental study of a compressive-mode energy harvester under random excitations. Smart Mater Struct 2017;26:035064.
[30] Vinson JR, Sierakowski RL. The behavior of structures composed of composite materials. Netherlands Springer; 2008.
[31] IEEE standard on piezoelectricity. New York: IEEE; 1987.